Microwave spectroscopy of the cold rubidium $(n+1)d_{5/2} \to ng$ and nh transitions

Jeonghun Lee,[1,*] J. Nunkaew,[2,†] and T. F. Gallagher[1]

[1]*Department of Physics, University of Virginia, Charlottesville, Virginia 22904, USA*
[2]*Department of Physics and Materials Science, Faculty of Science, Chiang Mai University, Chiang Mai 50200, Thailand*

We present an experimental technique that allows us to determine the zero-field intervals between high-ℓ states of Rb in a magneto-optical trap, in spite of the fact that we can only control the stray electric field in one direction. The technique is based on measuring a property of the atom that depends on the field, as opposed to its square. This approach allows the determination of the zero-field intervals and the magnitude of the stray field in the uncontrolled perpendicular direction. We use this technique to observe the microwave transitions of rubidium from the $(n+1)d_{5/2}$ states to the ng and nh states of $27 \leqslant n \leqslant 30$. From the observed microwave transitions, we determine the quantum defects of the ng and nh states. Using the quantum defects of the ng and nh states and the adiabatic core polarization theory, we determine the Rb$^+$ ionic dipole and quadrupole polarizabilities to be $\alpha_d = 9.12(2)a_0^3$ and $\alpha_q = 14(3)a_0^5$, respectively.

I. INTRODUCTION

Precise values for the quantum defects of the high angular momentum states are important in the calculations of the Stark effect, which are particularly important for Förster resonant dipole-dipole energy transfer involving Rydberg atoms [1–3]. Moreover, the ionic dipole and quadrupole polarizabilities of atoms can be determined from the same quantum defects since they arise from polarization of the core [4]. The dipole polarizabilities of alkaline-earth ions are of interest for clock applications and the dipole polarizabilities of alkali-metal atoms are of interest as benchmarks for atomic structure calculations relevant to parity-violation measurements and atom interferometry [5–10]. While most of the polarizability of the ground state of an alkali-metal atom is due to the valence electron, the contribution of the ionic core is not insignificant. For example, the Rb$^+$ dipole polarizability represents 3% of the Rb $5s$ ground-state polarizability [11]. For this reason, it is important to measure the dipole polarizabilities of alkali-metal ions.

Previous experimental values for the Rb$^+$ dipole and quadrupole polarizabilities were determined from the Rb nf and ng quantum defects in spite of the inverted fine structure of the nf states [12,13], the typical signature of the highest-ℓ core penetrating state [14]. Here ℓ is the orbital angular momentum of the Rydberg electron. A third measurement used only the nf series, and it is difficult to extract the polarizabilities from one ℓ series [15]. In all cases, the residual core penetration of the nf series leads to a large uncertainty in the Rb$^+$ dipole and quadrupole polarizabilities in previous work [12,13,15]. To obtain better values for the core polarizabilities it would be desirable to measure the quantum defects of nonpenetrating $\ell > 3$ states. However, as ℓ is increased the intervals between the ℓ states decrease and the Stark shifts due to small stray fields become a significant problem. To observe the intervals in zero field the field must be nulled in all directions. However, it is often the case that in an existing apparatus the field can only be nulled in one direction, leaving an unknown field

in the plane perpendicular to that direction and an unknown frequency shift.

Here we report the use of an experimental technique to determine zero-field intervals in spite of the fact that we can only null the field in one direction. Specifically, we measure a low-field parameter that depends on the static field E_S, not its square E_S^2. This approach enables us to determine the remaining perpendicular field and extrapolate the observed frequencies to zero field. We have used this approach to measure the Rb zero-field $(n+1)d_{5/2} \to ng$ and nh intervals. We are not able to resolve the ng and nh fine-structure intervals. Based on the ℓ dependence of the fine-structure intervals in other alkali-metal atoms, we expect them to be close to the hydrogenic $28g$ and $28h$ states, which are, respectively, 0.40 and 0.27 MHz for hydrogen [16–19]. Combining these intervals with the known Rb nd quantum defects, we derive the quantum defects of the Rb ng and nh states of $27 \leqslant n \leqslant 30$. From these quantum defects we extract substantially improved values for the Rb$^+$ ionic dipole and quadrupole polarizabilities. In the sections that follow we describe the principle of the approach, the experimental method, our observations, and the core polarization analysis.

II. PRINCIPLE

To illustrate the principle of the approach, as an example we describe extracting the zero-field $(n+1)d_{5/2} \to ng$ intervals. The Stark shifts of the levels and the frequency shift of the $(n+1)d_{5/2} \to ng$ transition are proportional to E_S^2 the squared magnitude of the static field E_S. It is convenient to write E_S^2 as

$$E_S^2 = E_z^2 + E_\perp^2, \tag{1}$$

where the field $\vec{E}_\perp$ lies in the plane perpendicular to the z direction. The frequency $\nu_{d_{5/2} \to g}$ of the $(n+1)d_{5/2} \to ng$ transition is given by

$$\nu_{d_{5/2} \to g} = \nu_{0,d_{5/2} \to g} + P E_S^2, \tag{2}$$

where P is half the difference in the polarizabilities of the d and g states and $\nu_{0,d_{5/2} \to g}$ is the zero-field interval. The direction

*jl7rf@virginia.edu
†Corresponding author: jn8h@virginia.edu

of $\vec{E}_S$ is unimportant. By applying the bias voltage V_b we are able to control the static field in the z direction (E_z), and if we measure the resonance frequency as a function of bias voltage V_b, or bias field E_b, we observe a parabola, with the maximum frequency $\nu_{0,d_{5/2}\to g} + P E_\perp^2$. This procedure leaves us with an unknown frequency shift of $P E_\perp^2$ because we cannot extrapolate E_S^2 to zero if only E_z is altered, as shown by Eq. (1).

In contrast, if we measure a property X that is simply related to E_S, given explicitly by

$$E_S = \sqrt{E_z^2 + E_\perp^2}, \qquad (3)$$

we can extrapolate to $E_S = 0$ and determine $E_\perp^2$. As an example, we consider the case in which X is proportional to E_S. The procedure is to measure the resonance frequency $\nu_{d_{5/2}\to g}$ and X as functions of V_b, or E_b, and plot $\nu_{d_{5/2}\to g}$ vs X^2. The observed frequencies should fall on a straight line, as shown by Eq. (2), and the $X^2 = 0$ intercept is the zero-field $(n+1)d_{5/2} \to ng$ interval.

The challenge is to identify the appropriate property X, and we have explored two different ones. In the first approach, X is the separation between Stark states. We take advantage of the fact that, for the high-ℓ states, the quantum defects are very small. Therefore, the zero-field ℓ states are converted to Stark k states, which exhibit linear Stark shifts, even in very small electric fields. A Stark state is assigned the label k, equal to the ℓ of the zero-field state to which it is adiabatically connected. The separation between adjacent Stark states $\Delta\nu_S = 3nE_S$ is linear in the field E_S [20]. We observe the microwave transitions from the $(n+1)d_{5/2}$ states to the nk Stark states and implicitly determine E_S from $\Delta\nu_S$, the separation between adjacent Stark states. For each bias voltage we obtain the value of $\Delta\nu_S$ from the Stark spectrum and we measure the $(n+1)d_{5/2} \to ng$ resonance frequency $\nu_{d_{5/2}\to g}$. Plotting the measured frequency $\nu_{d_{5/2}\to g}$ vs $\Delta\nu_S^2$ allows extrapolation to the zero-field interval, as shown by Eq. (2). An attractive feature of this approach is that only frequencies are measured.

In the second approach, X is the amplitude of the resonance signal. This method is based on the electric resonance method, first used in molecular beams to observe electric dipole transitions between states of the same parity [21]. It has also been used to measure Rydberg fine-structure intervals using radio-frequency electric fields [22]. The essential idea is that the (on-resonance) Rabi frequency Ω for the transition is proportional to the static field E_S; i.e., $\Omega \propto E_S$. In the presence of the static field E_S a single microwave photon can be used to drive the $(n+1)d_{5/2} \to ng$ transition and the Rabi frequency is given by

$$\Omega = \frac{\langle(n+1)d|\mu E_{mw}|nf\rangle\langle nf|\mu E_S|ng\rangle}{W_{ng} - W_{nf}}, \qquad (4)$$

from which it is evident that if E_{mw} is fixed, $\Omega \propto E_S$. We ignore the small variations due to the relative orientations of $\vec{E}_S$ and $\vec{E}_{mw}$.

If the microwave field is present for a time T, and $\Omega T \ll \pi$, then the transition probability, as well as the magnitude of the $(n+1)d_{5/2} \to ng$ resonance signal S, is proportional to $(\Omega T)^2$, which is proportional to E_S^2, so in this case $X \propto E_S^2$.
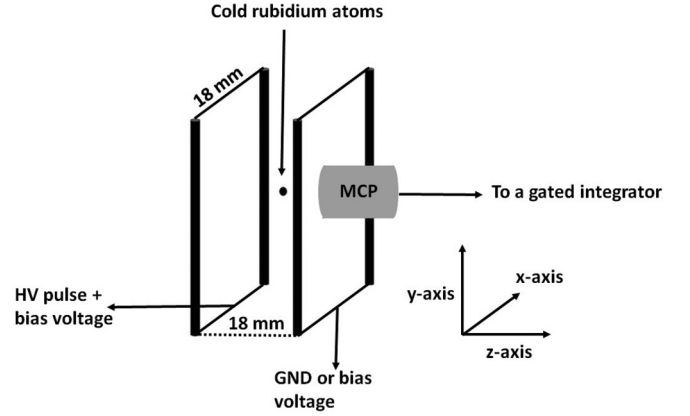

FIG. 1. The MOT configuration of this experiment.

In sum,

$$S \propto E_S^2. \qquad (5)$$

A plot of the resonance frequency $\nu_{d_{5/2}\to g}$ vs S should be a straight line, the intercept of which is the zero-field $(n+1)d_{5/2} \to ng$ interval. As we will see, this method, which requires lower fields and thus smaller extrapolations, is the preferred approach.

III. EXPERIMENTAL APPROACH

In the experiment, ^{85}Rb atoms in a vapor-loaded magneto-optical trap (MOT) are held at the center of four vertical rods as shown in Fig. 1 [23]. The rods pass through the corners of a horizontal square, 18 mm on a side. The two rods opposite the microchannel plate (MCP) detector are connected together (inside the vacuum chamber) and are used primarily to apply a field ionization pulse, although a dc bias voltage can also be applied. The two rods closest to the MCP are also connected together and can be grounded or biased to provide a static field.

The direction of the applied field is horizontal and parallel to the axis of the MCP. For simplicity, throughout this paper, we define the horizontal axis along the static electric field as the z direction as shown in Fig. 1. With this rod configuration, which is functionally equivalent to a pair of plates, we can only null the stray field in the z direction.

The 780-nm trap lasers are on continuously and Rb $5p_{3/2}$ atoms in the MOT are excited to the Rydberg $(n+1)d_{5/2}$ states by the a 10-μJ 480-nm laser pulse at a 20-Hz repetition rate. The laser pulse is 10 ns long with a bandwidth of 150 MHz. The trap magnetic fields are switched off ~4 ms before the laser pulse is fired. The trap fields in the MOT have fallen to less than 50 mG by the time the pulsed laser fires. After the laser is fired, atoms are exposed to the 500-ns microwave pulse to drive the $(n+1)d_{5/2} \to ng$ and nh transitions, as shown in Fig. 2. The continuous microwaves are generated by an Agilent E824C PSG CW synthesized signal generator, which produces frequencies up to 20 GHz. The microwaves are then formed into a 500-ns pulse by a General Microwave DM862B switch. The microwave frequency is doubled by a Narda 2640X220 active doubler and then tripled by Pacific Millimeter W3WO passive tripler to reach frequencies in the range of 75–110 GHz. The microwave pulse propagates through WR10 waveguide
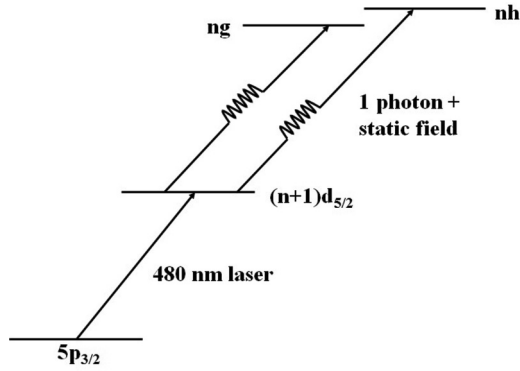
FIG. 2. Schematic of the Rydberg energy levels of this experiment.

and is launched from outside the vacuum chamber into the MOT volume by the WR10 horn. The polarization of the microwave field is nominally in the z direction, although, due to scattering from the rods, the polarization is not well known when the microwaves reach the atoms in the MOT. During the experiment the applied static electric field is always present. We ionize the Rydberg atoms and detect ions by applying a 3-μs rise time positive high-voltage pulse to the rods ~ 50 ns after the end of the microwave pulse. The resulting ions are driven to the MCP detector. The signal from the MCP is recorded with a gated integrator and stored in a computer for analysis.

IV. EXPERIMENTAL OBSERVATIONS AND DISCUSSION

A. Comparison of methods for determining the zero-field $(n + 1)d_{5/2}$-ng intervals

In this subsection we use the $29d_{5/2} \rightarrow 28g$ transition as a concrete example of different approaches to finding the zero-field intervals. Since the MOT configuration allows us to control the static field in only one direction $(\vec{E}_z)$, we first observe the frequency of the $29d_{5/2} \rightarrow 28g$ transition as a function of bias voltage applied to the rods, changing the field in the z direction from positive to negative. Although $d_{5/2} \rightarrow g$ transitions are more commonly driven as two microwave photon transitions [17], we drive them using one microwave photon and a static field, which we can vary by changing the bias voltage V_b. The observed frequencies of the resonances show the expected quadratic dependence on the bias voltage, as shown in Fig. 3. Fitting the observed frequencies to a quadratic dependence on the bias voltage gives 104 371.08(40) MHz as the maximum frequency at a bias voltage of $V_b = V_0 = 0.24$ V and 104367.74(40) MHz as the frequency when there is no bias voltage ($V_b = 0$). At $V_b = V_0 = 0.24$ V the stray field in the z direction is nulled. For our rod geometry the conversion between bias voltage and bias field, the correction to E_z, at the MOT is $E_b = 0.406V_b$ (with E_b in units of V/cm and V_b in V). Accordingly, the original stray field in the z direction is 97 mV/cm, which leads to frequency shift of 3.34 MHz. The frequency 104 371.08 MHz is only a lower limit to the $29d_{5/2}$-$28g$ frequency since the stray field in the x-y plane, $E_\perp$, is unknown. One might reasonably assume that the original stray field had approximately equal components in all three directions, in which case the uncompensated stray field would be 137 mV/cm, leading to an additional frequency shift
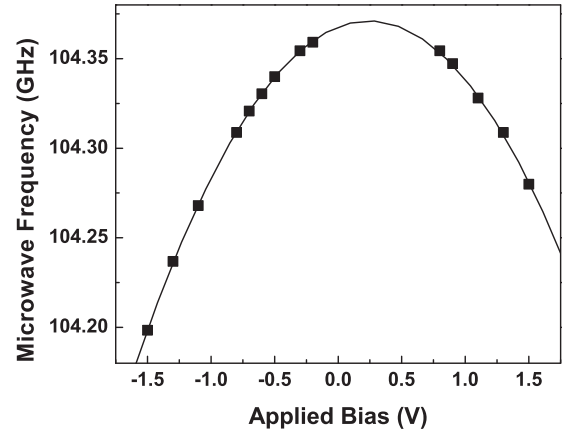

FIG. 3. Frequency of the microwave $29d_{5/2} \rightarrow 28g$ transition vs bias electric field in the z direction. The maximum frequency is 104 371.08(40) MHz at a bias voltage of $V_b = V_0 = 0.24$ V. At this bias, E_z is nulled.

of 6.68 MHz. Correcting for this assumed uncompensated shift gives a zero-field $29d_{5/2}$-$28g$ interval of 104 377.76 MHz. Assigning an uncertainty presents a problem, but an uncertainty equal to the correction for $E_\perp$, 6.7 MHz, does not seem unreasonable, yielding 104 377.8(67) MHz as the final result for the zero-field interval.

To take into account the fields in all directions we use the approaches described in Sec. II. In the first approach we implicitly determine E_S from $\Delta\nu_S$, the separation of adjacent Stark states. For each bias voltage we observe a Stark spectrum, as shown in Fig. 4(a), and the $d_{5/2} \rightarrow g$ transition with a lower microwave power in Fig. 4(b). The $d_{5/2} \rightarrow g$ transition also appears in Fig. 4(a), but it is power broadened when the high-k states are visible. The frequency separation $\Delta\nu_S$ between adjacent Stark states is proportional to E_S. For each bias voltage we obtain values of the $d_{5/2} \rightarrow g$ frequency $\nu_{d_{5/2} \rightarrow g}$ and $\Delta\nu_S$, taken from the high-k states indicated in Fig. 4(a). From these pairs of points we construct the parametric plot of the $d_{5/2} \rightarrow g$ frequency vs $\Delta\nu_S^2$. As shown in Fig. 5, the result is a straight line, as expected from Eq. (2), and its intercept is the zero field $d_{5/2} \rightarrow g$ interval. From Fig. 5, we obtain the zero-field $29d_{5/2} \rightarrow 28g$ transition frequency to be 104 378.9(62) MHz.

This approach has the attraction that we are measuring frequencies, but it has the obvious problem that the fields must be large enough to obtain good values for the separation between the Stark states. The relatively large fields require a long extrapolation, 40 MHz, to zero field and they introduce the possibility that the Stark shift of the transition frequency may not be adequately represented by Eq. (2). A variant of this technique is to conduct the Stark spectroscopy at higher n, where the separations are larger, allowing the use of smaller fields. This approach has been used by Stevens and Lundeen to monitor static fields [24].

To conduct measurements in lower static fields we use the second approach described in Sec. II. Specifically, we measure the signal amplitude S of the $(n + 1)d_{5/2} \rightarrow ng$ transition at different bias voltages. Since we are driving the transition with one microwave photon and a static field, for a fixed microwave amplitude the Rabi frequency is proportional to the static field,
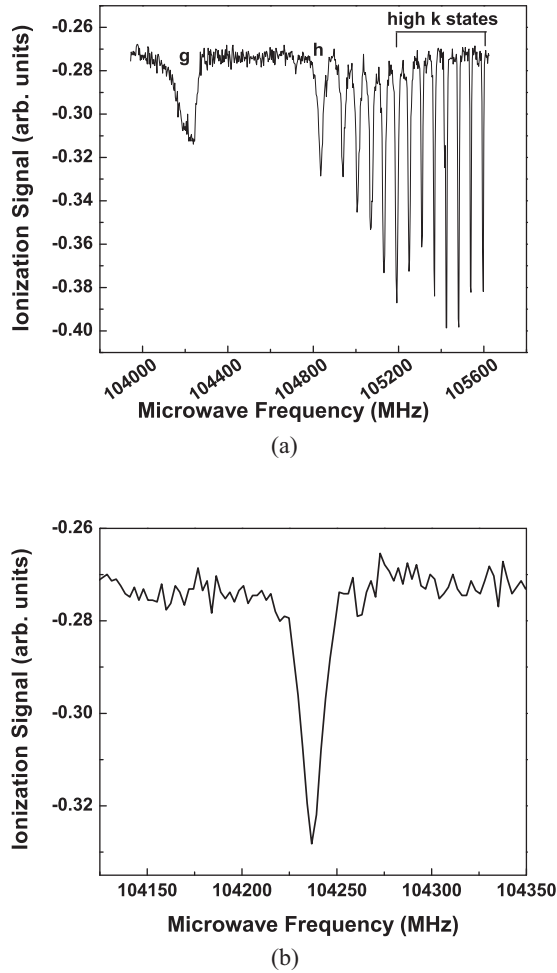
FIG. 4. (a) The $29d_{5/2} \rightarrow 28k$ Stark spectrum at a bias voltage of $V_b = -1.3$ V at the relative microwave power 1. The high-k states are indicated in the graph. (b) The $29d_{5/2} \rightarrow 28g$ transition at the same bias field as (a) but a relative microwave power of 0.032.
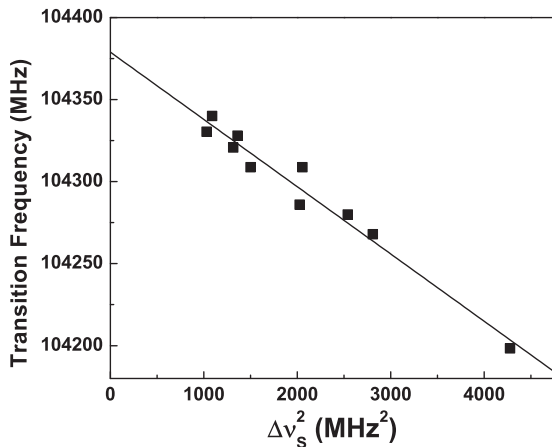

FIG. 5. The $29d_{5/2} \rightarrow 28g$ transition frequency vs the square of the Stark splitting of the high-k states $\Delta\nu_S^2$ obtained from Stark spectroscopy. At $\Delta\nu_S^2 = 0$, the stray field is zero and the $29d_{5/2} \rightarrow 28g$ transition frequency is 104 378.9(62) MHz.
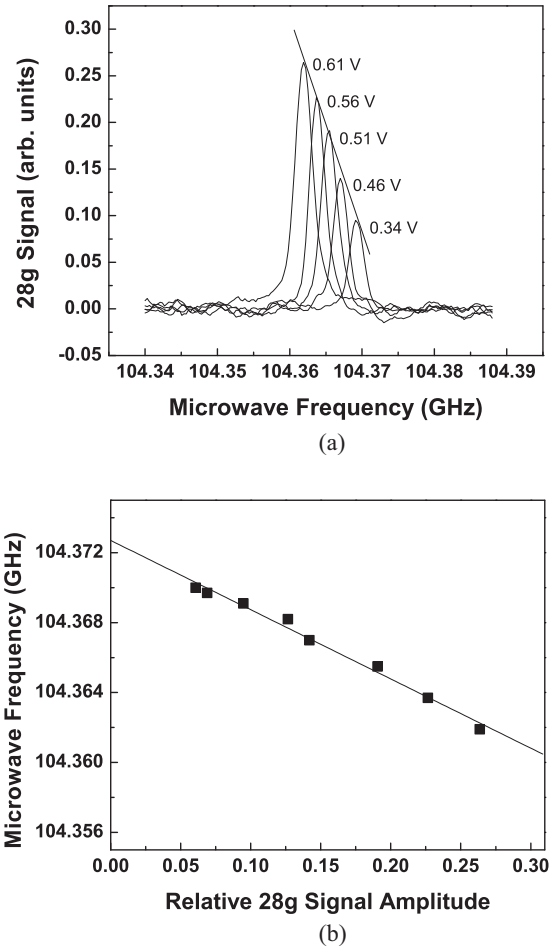

FIG. 6. (a) Observed $29d_{5/2} \rightarrow 28g$ resonance signals with different bias voltages. As shown by the slanted line, the signal amplitude varies linearly with the observed resonance frequency. The resonance frequency increases and the signal amplitude decreases as the bias voltage is reduced from $V_b = 0.61$ V to 0.34 V, which reduces E_z from 150 mV/cm to 41 mV/cm. (b) The $29d_{5/2} \rightarrow 28g$ microwave transition frequency as a function of the relative $28g$ signal amplitude. From the graph, the $29d_{5/2} \rightarrow 28g$ transition frequency at zero stray field is 104 372.70(28) MHz.

as shown by Eq. (4). The experiment is conducted in the low-transition-probability regime in which S is proportional to E_S^2. The procedure is similar to that used for the Stark spectroscopy approach. For each bias voltage we observe the $d_{5/2} \rightarrow g$ resonance, as shown in Fig. 6(a) for bias voltages between 0.34 and 0.61 V. As shown by Fig. 6(a), the signal amplitude S increases and the resonance frequency $\nu_{d_{5/2} \rightarrow g}$ shifts with increasing bias voltage. Since $S \propto E_S^2$, a parametric plot of $\nu_{d_{5/2} \rightarrow g}$ vs S yields a straight line, the intercept of which is the zero-field $d_{5/2} \rightarrow g$ frequency as shown in Fig. 6(b). From Fig. 6(b) the zero-field $29d_{5/2} \rightarrow 28g$ frequency is 104 372.70(28) MHz. The extrapolation in this method is ~ 4 MHz, which is much less than the aforementioned approach, which results in a smaller uncertainty in determining the the zero-field $29d_{5/2} \rightarrow 28g$ frequency.

In Fig. 6 we have not explicitly used the bias voltages, but from them we can extract the values of the perpendicular stray field. When the observed frequencies are plotted vs the
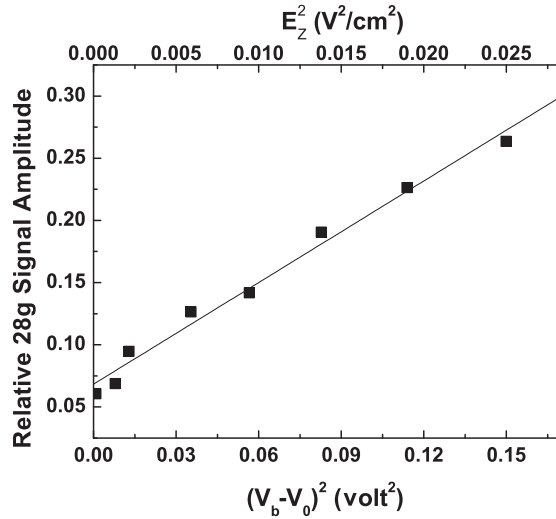
FIG. 7. Graph of the relative $28g$ signal amplitude S as a function of squared voltage $(V_b - V_0)^2$ and squared static field E_z^2 in the z direction of the system. Since $S = a(E_z^2 + E_\perp^2)$, from the intercept and slope of the graph we determine $E_\perp$ to be 91 mV/cm.

bias voltages V_b we obtain a parabola similar to Fig. 3, with the maximum frequency of 104 369.87(44) MHz occurring at $V_b = V_0 = 0.875$ V. Since S is proportional to E_S^2, we write

$$S = aE_S^2 = a\left(E_z^2 + E_\perp^2\right), \tag{6}$$

where a is a constant. In Fig. 7 we plot S vs $(V_b - V_0)^2$, which is in effect a plot of S vs E_z^2, as shown by the horizontal scale at the top of the figure. At the S intercept of the graph $E_z = 0$ and $E_S^2 = E_\perp^2$. The slope $a = dS/dE_S^2$; combining these two values from Fig. 7, we obtain $E_\perp = 91$ mV/cm. We can check this value for $E_\perp$ using a different approach. With $V_b = 0$ the observed frequency is 104 326.05 MHz; $V_b = V_0 = 0.875$ V, so that $E_z = 0$ mV/cm, results in a shift of 43.82 MHz. To reach the zero-field value requires a further shift of 2.83 MHz, which implies that $E_\perp = 90$ mV/cm, in good agreement with the value given above. It is instructive to apply the same method of analysis to the data of Fig. 3, which leads to $E_\perp = 68$ mV/cm. The data shown in Figs. 3 and 6 were taken with opposite polarity field ionization pulses, which result in different bias fields in the z direction. Nonetheless, the values for $E_\perp$ are similar. In addition, the values for $E_\perp$ are smaller than the bias field in the z direction due to the fact that the bias field in the z direction is determined by an external circuit.

At this point it is useful to compare the three approaches we have described. The first method, measuring transition frequency as a function of bias voltage, allows the determination of the $29d_{5/2} \rightarrow 28g$ frequency with high precision, but the observed frequency is the zero-field $29d_{5/2}$-$28g$ interval altered by an unknown Stark shift due to the uncanceled stray field $E_\perp$. Estimating the Stark shift due to $E_\perp$ by assuming that the magnitudes of the stray field $|E_x|$, $|E_y|$, and $|E_z|$ are the same, we arrive at a zero-field $29d_{5/2}$-$28g$ interval of 104 377.8(67) MHz. The second method, measuring transition frequency as a function of separation of adjacent Stark states, yields a $29d_{5/2} \rightarrow 28g$ frequency transition of 104 378.9(62) MHz. This method has the distinct advantage of actually measuring $|E_\perp|$, but it has the disadvantage of requiring a long

TABLE I. The $(n + 1)d_{5/2} \rightarrow ng$ microwave transition frequencies in zero electric field and the extracted quantum defects of ng.

n	Transition frequency (MHz)	Quantum defect
27	116 464.54(35)	0.0039737(11)
28	104 372.70(28)	0.0039701(10)
29	93 895.75(34)	0.0039746(13)
30	84 775.26(65)	0.0039778(27)

extrapolation to zero field, which results in an uncertainty of 6.2 MHz, not really much better than the estimated uncertainty of the first method. The third method, measuring transition frequency as a function of the signal amplitude, yields a $29d_{5/2} \rightarrow 28g$ frequency transition of 104 372.70(28) MHz. The shorter extrapolation results in a smaller uncertainty, 0.28 MHz, of the the zero-field $29d_{5/2} \rightarrow 28g$ frequency and using this method we estimate $E_\perp$ to be 91 mV/cm, slightly less than our estimate of 137 mV/cm made on the basis of simply measuring the frequency vs the bias voltage V_b. Comparing the three methods shows that the third method, unlike the first method, has a known uncertainty and it is a factor of 20 smaller than the uncertainty of the second method. Consequently, we use the third method to determine the zero-field intervals in the sections that follow. Finally, we note that, although the stray field varies from day to day, the zero field intervals extracted remain constant, within their uncertainties.

B. The $(n + 1)d_{5/2}$-ng intervals and ng quantum defects

While measuring signal strengths is less appealing than measuring frequencies, as in the separation between the Stark states, the much lower static fields make the signal amplitude method more attractive and we have used it to measure the $(n + 1)d_{5/2} \rightarrow ng$ transition frequencies for $27 \leqslant n \leqslant 30$, as shown in Table I. To find the quantum defects of the ng states, we add the known quantum defects of the nd states from Ref. [25] and the $(n + 1)d_{5/2} \rightarrow ng$ transition frequencies. The values of the quantum defects of the ng states of $27 \leqslant n \leqslant 30$ are shown in Table I. References [12,13,26] measured quantum defects of the ng states to be 0.004 00(9), 0.004 05(6), and 0.004 02(8), respectively. References [12,13] did not consider n dependence and Ref. [26] measured only the $30g$ quantum defect. As seen from Table I, our values of the quantum defect have improved upon the previous measurements by an order of magnitude. Our quantum defects show a slight n dependence and we fit them to a Ritz formula

$$\delta_g = \delta_0 + \frac{\delta_1}{(n - \delta_0)^2}, \tag{7}$$

which yields the values $\delta_0 = 0.004\,00(2)$ and $\delta_1 = -0.018(15)$.

C. The $(n + 1)d_{5/2}$-nh intervals and nh quantum defects

We obtain the zero-field $(n + 1)d_{5/2} \rightarrow nh$ intervals in much the same way as we obtained the $(n + 1)d_{5/2} \rightarrow ng$ intervals. We drive the $d_{5/2} \rightarrow h$ transitions using one microwave photon and a static field. The Rabi frequency Ω
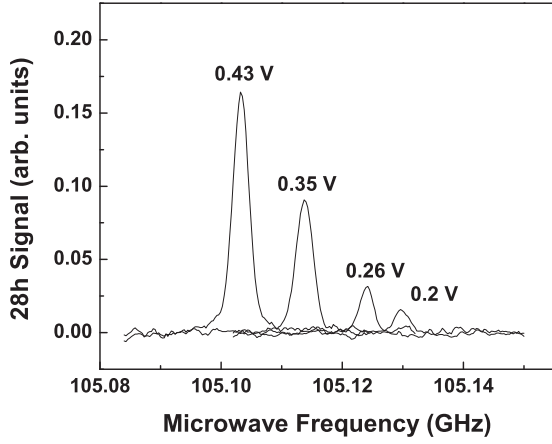
FIG. 8. Observed amplitude as the $29d_{5/2} \rightarrow 28h$ resonance changes in different bias voltages.

is given by

$$\Omega = \frac{\langle d|\mu E_{mw}|f\rangle\langle f|\mu E_s|g\rangle\langle g|\mu E_s|h\rangle}{(W_{ng} - W_{nf})(W_{nh} - W_{ng})}. \qquad (8)$$

In this case $\Omega \propto E_S^2$ and in the low-transition-probability regime $S \propto E_S^4$. The experiment is conducted in much the same way as the $d_{5/2} \rightarrow g$ measurements; for different bias voltages the signal amplitude S and resonance frequency $\nu_{d_{5/2} \rightarrow h}$ are measured while keeping the microwave field amplitude fixed. Figure 8 shows the $29d_{5/2} \rightarrow 28h$ transition as an example. A parametric plot of $\nu_{d_{5/2} \rightarrow h}$ vs $\sqrt{S}$ should give a straight line, the intercept of which is the zero-field $d_{5/2} - h$ interval, and in Fig. 9 we present this plot for the $29d_{5/2} \rightarrow 28h$ transition. As shown, the plot matches our expectation and yields the zero-field interval of 105 140.87(77) MHz. Following the same procedure we have measured the $(n + 1)d_{5/2} \rightarrow nh$ intervals for $28 \leqslant n \leqslant 30$, with the results shown in Table II. In Table II we also give the nh quantum defects, obtained in a manner analogous to that used to obtain the ng quantum defects.
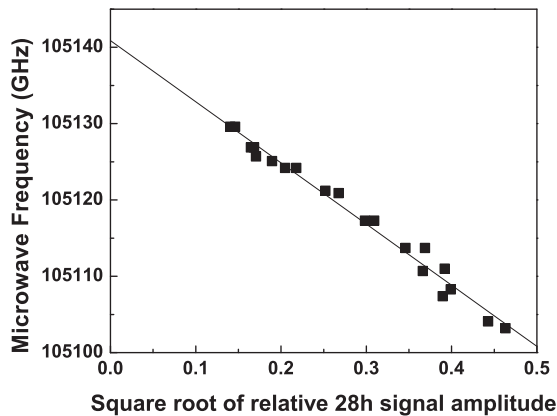

FIG. 9. Frequency of the observed $29d_{5/2} \rightarrow 28h$ resonances as a function of the square root of the relative $28h$ signal amplitude $\sqrt{S}$. From the graph, the $29d_{5/2} \rightarrow 28h$ transition frequency at zero field is 105 140.87(77) MHz.

TABLE II. The $(n + 1)d_{5/2} \rightarrow nh$ microwave transition frequencies in zero electric field and the extracted quantum defects of nh.

n	Transition frequency (MHZ)	Quantum defect
28	105 140.9(8)	0.0014078(27)
29	94 591.0(22)	0.0013982(82)
30	85 400.3(15)	0.0014137(62)

D. The Rb⁺ ionic dipole and quadrupole polarizabilities

We use the values of quantum defects that we have determined and the adiabatic core polarization model of Mayer and Mayer to extract the ionic dipole and quadrupole polarizabilities of Rb⁺ [4]. For the high-ℓ states, where $\ell > 3$, the energy levels of the Rb atoms are depressed from the hydrogenic levels only by core polarization; core penetration is negligible. In Rb the Rydberg electron moves much more slowly than the electrons in the core and the Rb⁺ core is polarized by the slowly varying field from the Rydberg electron. The polarization interaction between the Rydberg electron and the ion core depresses the energy of the Rb $n\ell$ Rydberg state below the energy of a hydrogenic $n\ell$ state by

$$W_{pol,n\ell} = -\frac{\alpha_d}{2}\langle 1/r_{n\ell}^4\rangle - \frac{\alpha_q}{2}\langle 1/r_{n\ell}^6\rangle, \qquad (9)$$

where α_d and α_q are the ionic dipole and quadrupole polarizabilities. The expectation values $\langle 1/r_{n\ell}^4\rangle$ and $\langle 1/r_{n\ell}^6\rangle$ are the squares of the field and the field gradient of the Rydberg electron in the $n\ell$ state at the core. The resulting energy of the Rb $n\ell$ state is given by

$$W_{n\ell} = -1/2n^2 + W_{pol,n\ell}. \qquad (10)$$

The energy levels of the Rydberg $n\ell$ state can also be expressed as
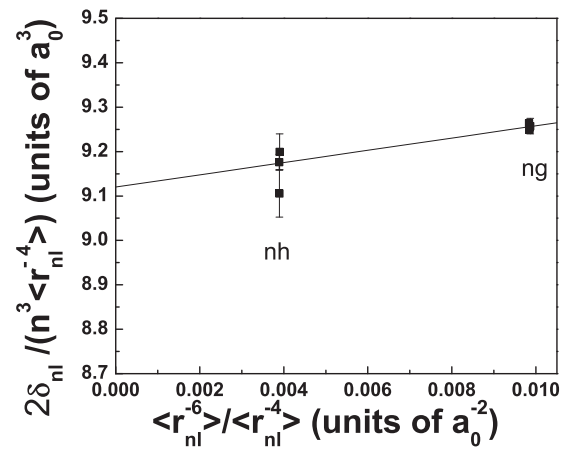
$$W_{n\ell} = -1/2(n - \delta_{n\ell})^2, \qquad (11)$$

FIG. 10. Plot of the measured ng and nh quantum defects scaled by $n^3\langle r_{n\ell}^{-4}\rangle/2$ vs $\langle r_{n\ell}^{-6}\rangle/\langle r_{n\ell}^{-4}\rangle$ using Eq. (14). There are three data points for the nh quantum defects $28 \leqslant n \leqslant 30$ and four data points for the ng quantum defects $27 \leqslant n \leqslant 30$. A fit to the straight line yields the y intercept and slope, which are α_d and α_q, respectively. The resulting fit values are $\alpha_d = 9.12(2)a_0^3$ and $\alpha_q = 14(3)a_0^5$.

TABLE III. The Rb$^+$ dipole (α_d) and quadrupole (α_q) polarizabilities obtained from this work and other theoretical (Theor.) and experimental (Expt.) results.

α_d (a_0^3)	α_q (a_0^5)
This work	
9.12(2)	14(3)
Other works	
$8.9 < \alpha_d < 9.3$ (Expt.) [12]	$0 < \alpha_q < 43$ (Expt.) [12]
$8.5 < \alpha_d < 9.7$ (Expt.) [13]	$0 < \alpha_q < 55$ (Expt.) [13]
8.98 (Expt.) [15]	35.4 (Theor.) [11]
9.1 (Theor.) [11]	38.37 (Theor.) [29]
9.11 (Theor.) [30]	35.41 (Theor.) [31]
9.076 (Theor.) [31]	

where $\delta_{n\ell}$ is the quantum defect of the Rydberg $n\ell$ state. Since n is much larger than $\delta_{n\ell}$, using a Taylor expansion we can express the polarization energy as

$$W_{\text{pol},n\ell} = 1/2n^2 + W_{n\ell} \cong -\frac{\delta_{n\ell}}{n^3}. \tag{12}$$

From Eqs. (9) and (12) we get

$$\frac{\delta_{n\ell}}{n^3} = \frac{\alpha_d}{2}\langle 1/r_{n\ell}^4 \rangle + \frac{\alpha_q}{2}\langle 1/r_{n\ell}^6 \rangle. \tag{13}$$

We can rewrite Eq. (13) as

$$2\frac{\delta_{n\ell}}{n^3 \langle 1/r_{n\ell}^4 \rangle} = \alpha_d + \alpha_q \frac{\langle 1/r_{n\ell}^6 \rangle}{\langle 1/r_{n\ell}^4 \rangle}. \tag{14}$$

Equation (14) implies that a graph of $2\delta_{n\ell}/(n^3\langle r_{n\ell}^{-4}\rangle)$ vs $\langle r_{n\ell}^{-6}\rangle/\langle r_{n\ell}^{-4}\rangle$ is linear, with α_d as the intercept and α_q as the slope of the graph. Here the values of $\delta_{n\ell}$ are the experimentally determined values given above for $27 \leqslant n \leqslant 30$, $l = 4$ and 5. We use the known analytic expressions for $\langle r_{n\ell}^{-4}\rangle$ and $\langle r_{n\ell}^{-6}\rangle$ for the $n\ell$ states of hydrogen [27,28]. In Fig. 10 we plot the graph of $2\delta_{n\ell}/(n^3\langle r_{n\ell}^{-4}\rangle)$ vs $\langle r_{n\ell}^{-6}\rangle/\langle r_{n\ell}^{-4}\rangle$ and we determine the ionic dipole and quadrupole polarizabilities to be $\alpha_d = 9.12(2)a_0^3$ and $\alpha_q = 14(3)a_0^5$, respectively. In Table III we compare the Rb$^+$ ionic dipole and quadrupole polarizabilities obtained from our work to other theoretical and experimental work. Our ionic dipole polarizability agrees with the earlier experimental determinations, but has a much smaller uncertainty, and it agrees very well with the theoretical predictions. References [6,11] contain excellent summaries of the theory of ionic polarizabilities. The experimental values for the ionic dipole polarizability from Refs. [12,13,15] are determined from the nf and ng energy levels using the core polarization model. Although the nf states are core penetrating states that should not be treated using the core polarization analysis alone, the values obtained for α_d are consistent with ours.

Our ionic quadrupole polarizability falls within the broad limits set in Refs. [12,13] but is about a factor of 2 lower than the theoretical prediction. In the latter connection it is noteworthy that core polarization analyses of Rydberg quantum defects of other elements have consistently yielded ionic quadrupole polarizabilities that are lower than theoretically predicted [16,32–35]. It is a worthy theoretical challenge to pinpoint the source of the discrepancy between the theoretical and experimental values. We believe that the core polarization model needs to be reexamined closely.

V. CONCLUSION

We have presented an experimental technique to determine zero-field transition frequencies in spite of our inability to completely cancel the stray field. We use the technique to measure the microwave transition frequencies from the Rydberg $(n + 1)d_{5/2}$ states to the Rydberg ng and nh states, $27 \leqslant n \leqslant 30$. The ng and nh quantum defects of the measured n states are determined from the observed microwave transition frequencies. We extract the Rb$^+$ dipole and quadrupole polarizabilities from the values of quantum defects to be $\alpha_d = 9.12(2)a_0^3$ and $\alpha_q = 14(3)a_0^5$, respectively. The Rb$^+$ dipole polarizability agrees well with recent theoretical values. However, the Rb$^+$ α_q is about a factor of 2 lower than the theoretical prediction. The discrepancy between theoretical and experimental values is consistent with the determined α_q of other elements using the core polarization analysis. We hope this work will motivate theoretical work to locate the source of discrepancy between the experimental and theoretical values of α_q in the core polarization analysis.

[1] P. Bohlouli-Zanjani, J. A. Petrus, and J. D. D. Martin, Phys. Rev. Lett. **98**, 203005 (2007).

[2] A. Reinhard, T. Cubel Liebisch, K. C. Younge, P. R. Berman, and G. Raithel, Phys. Rev. Lett. **100**, 123007 (2008).

[3] J. Nipper, J. B. Balewski, A. T. Krupp, B. Butscher, R. Löw, and T. Pfau, Phys. Rev. Lett. **108**, 113001 (2012).

[4] J. E. Mayer and M. G. Mayer, Phys. Rev. **43**, 605 (1933).

[5] H. Gould and T. M. Miller, Adv. At. Mol. Opt. Phys. **51**, 343 (2005).

[6] J. Mitroy, M. S. Safronova, and C. W. Clark, J. Phys. B **43**, 202001 (2010).

[7] C. R. Ekstrom, J. Schmiedmayer, M. S. Chapman, T. D. Hammond, and D. E. Pritchard, Phys. Rev. A **51**, 3883 (1995).

[8] A. Miffre, M. Jacquey, M. Büchner, G. Trénec, and J. Vigué, Phys. Rev. A **73**, 011603(R) (2006).

[9] M. D. Gregoire, I. Hromada, W. F. Holmgren, R. Trubko, and A. D. Cronin, Phys. Rev. A **92**, 052513 (2015).

[10] W. F. Holmgren, M. C. Revelle, V. P. A. Lonij, and A. D. Cronin, Phys. Rev. A **81**, 053607 (2010).

[11] M. S. Safronova and U. I. Safronova, Phys. Rev. A **83**, 052508 (2011).

[12] J. Han, Y. Jamil, D. V. L. Norum, P. J. Tanner, and T. F. Gallagher, Phys. Rev. A **74**, 054502 (2006).

[13] L. A. M. Johnson, Ph.D. thesis, University of Leeds, 2011.

[14] R. M. Sternheimer, J. E. Rodgers, and T. P. Das, Phys. Rev. A **17**, 505 (1978).

[15] I. Johansson, Ark. Fys. **20**, 135 (1961).

[16] W. E. Cooke, T. F. Gallagher, R. M. Hill, and S. A. Edelstein, Phys. Rev. A **16**, 1141 (1977).

[17] T. F. Gallagher, R. M. Hill, and S. A. Edelstein, Phys. Rev. A **14**, 744 (1976).

[18] L. G. Gray, X. Sun, and K. B. MacAdam, Phys. Rev. A **38**, 4985 (1988).

[19] N. H. Tran, H. B. van Linden van den Heuvell, R. Kachru, and T. F. Gallagher, Phys. Rev. A **30**, 2097 (1984).

[20] H. A. Bethe and E. A. Salpeter, *Quantum Mechanics of One- and Two-Electron Atoms* (Plenum, New York, 1977).

[21] H. K. Hughes, Phys. Rev. **72**, 614 (1947).

[22] T. F. Gallagher, L. M. Humphrey, R. M. Hill, W. E. Cooke, and S. A. Edelstein, Phys. Rev. A **15**, 1937 (1977).

[23] H. Park, P. J. Tanner, B. J. Claessens, E. S. Shuman, and T. F. Gallagher, Phys. Rev. A **84**, 022704 (2011).

[24] G. D. Stevens and S. R. Lundeen, Phys. Rev. A **60**, 4379 (1999).

[25] W. Li, I. Mourachko, M. W. Noel, and T. F. Gallagher, Phys. Rev. A **67**, 052502 (2003).

[26] K. Afrousheh, P. Bohlouli-Zanjani, J. A. Petrus, and J. D. D. Martin, Phys. Rev. A **74**, 062712 (2006).

[27] T. F. Gallagher, *Rydberg Atoms* (Cambridge University Press, Cambridge, 1994).

[28] K. Bockasten, Phys. Rev. A **9**, 1087 (1974).

[29] R. M. Sternheimer, Phys. Rev. A **1**, 321 (1970).

[30] I. S. Lim, J. K. Laerdahl, and P. Schwerdtfeger, J. Chem. Phys. **116**, 172 (2002).

[31] W. R. Johnson, D. Kolb, and K.-N. Huang, At. Data Nucl. Data Tables **28**, 333 (1983).

[32] K. A. Safinya, T. F. Gallagher, and W. Sandner, Phys. Rev. A **22**, 2672 (1980).

[33] J. Nunkaew, E. S. Shuman, and T. F. Gallagher, Phys. Rev. A **79**, 054501 (2009).

[34] E. G. Kim, J. Nunkaew, and T. F. Gallagher, Phys. Rev. A **89**, 062503 (2014).

[35] J. Nunkaew and T. F. Gallagher, Phys. Rev. A **91**, 042503 (2015).